BIRD IMPACT STUDY OF A PRELOADED COMPOSITE WIND TURBINE BLADE

N. Nanami*, O. O. Ochoa
Dept. of Mechanical Engineering, Texas A&M University, College Station, TX, USA
* Corresponding author (jhonn-2@tamu.edu)

Keywords: *large-scale wind turbine blades; CF/GF hybrid composite materials; coupled Eulerian-Lagrangian; implicit-explicit coupling; damage assessment; soft body impact*

Abstract

Composite wind turbine blades must sustain aerodynamic, inertial, and gravitational loads, as well as mitigate operational conditions in case of hail and bird strike. Herein we present a methodology for the damage assessment of bird impact on a preloaded composite wind turbine blade. Structural response of the blade is evaluated through finite element simulations addressing its static and dynamic behavior focusing on deformation, stresses, damage mechanisms, and energy absorption. The results of the 2kg-bird impact study revealed that the service loads of the 80 meter blade did not accelerate the damage progression. Overall conclusion is that the 5 meter tip-sectional blade of the computational study is an acceptable target structure for bird impact tests instead of the full scale blade.

1 Introduction

Wind energy market has grown rapidly in the last couple of decades with plans to commercially install large-scale wind turbines such as 8-12 MW class (160 m-190 m in a rotor diameter) [1]. Mostly, a horizontal-axis wind turbine (HAWT) with propeller type blades is utilized in such large-scale wind power system, and its configuration as an upwind land-based construction is schematically depicted in Fig. 1. In general, large-scale HAWTs have either two or three blades, with both cylindrical and airfoil cross-sections. Typically, the blade consists of an upper and a lower blade skin, spar cap, and shear web, which are bonded together as depicted in Fig. 2. The skin and web are usually of sandwich construction comprised of glass fiber (GF) fabric and/or unidirectional glass fiber (UD-GF) reinforced polymers for the face sheet and polymeric foams, balsa wood, or honeycomb type as the core material. For a large-scale HAWT blade, a hybrid carbon and glass fiber (CF/GF) composite spar cap laminate was often employed to resist flapping bending. Additionally, constant thickness was employed for the face sheet, and thickness of the core and spar cap laminate was defined as a function of the airfoil chord length [2-7]. The large and robust blade designs rely on hybrid material systems such as CF/GF reinforced composite materials to improve specific stiffness/strength and damage tolerance due to aerodynamic, inertia, gravitational, operational and impact loads.

The blade is often exposed to bird impact in addition to service loads [8]. Suitable approaches for impact simulations are either Lagrangian, Coupled Eulerian-Lagrangian (CEL), Arbitrary Lagrangian-Eulerian (ALE), or Smoothed-Particle Hydrodynamics (SPH) [9-11]. Since a bird is mostly composed of water, the artificial bird is akin to hydrodynamic representation with a simple geometry such as a cylinder, an ellipsoid, or a sphere [10-13]. Herein, a computational methodology for the bird impact response of the rotating blade is presented to assist the design process of the large-scale blades.

2 Blade Description

The blade of our 8MW wind turbine (SW45) is described in this section. The blade has a blade tip radius of 80 m and is positioned at a 140 m hub-height [1].

2.1 Geometry Specifics

After an extensive study of the open literature, the blade with sandwich skin, spar cap and shear web reinforcements is created based on the following non-dimensional specifications: The non-dimensional chord (c/R) distribution along the rotor radius is taken from Griffin [6]. The ratio of the blade thickness to the chord length (t/c) along the rotor radius are provided by Somers et al. [14]. Spar cap and shear web as internal reinforcements of the blade are constructed in the airfoil section (5.6 m < r < 80 m). To improve buckling stability in the blade, the forward and aft shear web are attached at the recommended positions [6]. Spar cap is located

between the forward and aft shear web. Dorsally the spar cap width remains constant between r = 5.6 m and r = 20 m, and this width is linearly decreased further to the blade tip.

The thick-airfoil family (NREL S817, S816, S818) is employed for the blade because of its excellent aerodynamic performance as reported [14]. Although practical wind turbine blades are pre-twisted along the rotor radius, the pre-twist angle distribution is neglected for simplicity in the present model.

2.2 Composite Layup

The root section (4 m < r < 5.6 m) of the blade consists of GF fabric layers. Since metallic bolts with a large diameter are installed into the blade root connected to the hub, this root section usually experiences high stresses which are mitigated with the selection of 40 mm thick laminate. In the airfoil section (5.6 m < r < 80 m), sandwich constructions of GF face sheets with balsa core are employed in the blade skin and shear web. The face sheet of the skin is GF fabric layer, and the face in the web is laminated with GF fabric and ±45° UD-GF layers. The hybrid composite spar cap laminate is composed of 15% CF fabric and 85% UD-GF layers by volume. Properties of both the skin and spar cap laminates are assigned to the skin between the forward and aft shear web, and these properties create the asymmetric section stiffness matrix as depicted in Fig. 2.

The thickness of the spar cap laminate and balsa core are determined as a function of the airfoil chord length. They are assigned as a step function to incorporate a gradual taper in laminate thickness. A constant thickness of the face sheet in sandwich constructions is employed and listed in Table 1.

2.3 Tip-Sectional Blade

A tip-sectional blade (TSB5M) is extracted from the final 5 m long section of the full-length SW45 blade without any modifications. All geometric specifications and laminate details used in the sectional blade are identical to those located between r = 75 m and r = 80 m of the SW45 blade.

3 Soft Body Impact Representation

3.1 Constitutive Model

An equation of state (EOS) material model is adopted as an approximation for the constitutive model of a bird (soft body impactor). In this linear model, pressure (p) is obtained from Eq. (1) which represents the coupling of pressure and internal energy [15]:

$$p = \frac{\rho_0 c_0^2 \eta}{(1 - s\eta)^2}\left(1 - \frac{\Gamma_0 \eta}{2}\right) + \Gamma_0 \rho_0 E_m \qquad (1)$$

where ρ_0 is the reference density; c_0, the bulk speed of sound; $\eta = 1 - \rho_0/\rho$, the nominal volumetric compressive strain; ρ, the current density; s and Γ_0, material constants; E_m, the specific energy. Note that $\rho_0 c_0^2$ is equivalent to the elastic bulk modulus at small nominal strains. The linear relationship between the shock velocity (U_s) and the particle velocity (U_p) is defined through s as expressed in Eq. (2).

$$U_s = c_0 + sU_p \qquad (2)$$

A deviatoric behavior uncoupled with volumetric response is introduced into the EOS material model to take into account the shear strength of an impactor. The deviatoric stress tensor ($\mathbf{S}$) for the Newtonian viscous shear behavior is expressed in Eq. (3) where η_v denotes the viscosity; $\dot{\mathbf{e}}$, the deviatoric part of a strain rate tensor [15].

$$\mathbf{S} = 2\eta_v \dot{\mathbf{e}} \qquad (3)$$

3.2 Representative Bird Geometry/Material

Since the irregular shape of a bird poses difficulties in impact problems, a cylinder composed of gelatin with hemispherical ends is selected for its representation [10-13]. The aspect ratio of 2, defined as the length (0.24 m) of the cylinder to its diameter (0.12 m), is adopted to provide a realistic impact pressure profile [16, 17]. The density of gelatin is 911 kg/m^3, resulting in a bird mass of 2.0 kg approximately. The properties of gelatin used in the simulations are as follows: $c_0 = 1.4829\times10^3$ m/s, s = 2.0367, $\Gamma_0 = 0$, $\eta_v = 4\times10^{-3}$ Ns/m^2 [13].

4. Damage and Failure Modes

Materials with reversible behavior are described by generalized Hooke's law. Hashin damage initiation criteria and energy-based damage evolution law are utilized to track various damage modes and mechanisms in the composite laminates while von Mises yield criteria is selected for isotropic core.

4.1 Progressive Damage in Composites

Hashin damage initiation criteria for the composites identify four different damage modes: fiber tension, fiber compression, matrix tension, and matrix compression [18, 19]. Damage initiation is detected when the initiation criteria reaches the value of 1. For the post-damage initiation behavior, the energy dissipation due to failure (G^C) is taken as the metric and calculated as expressed in Eq. (4) where ε_{eq}^f is the equivalent strain where the material is considered failure completely; σ_{eq}^0, the initial equivalent stress where the initiation criteria are met; L^c, characteristic length of an element. The characteristic length of an element is simply computed as the square root of the area associated with the element [20].

$$G^C = \varepsilon_{eq}^f \sigma_{eq}^0 L^c / 2 \qquad (4)$$

The effective stress tensor is obtained from the nominal stress tensor and damage operator tensor which embodies three internal damage variables (d_f, d_m, d_s) to portray fiber, matrix, and shear damage. Thus, it is used to monitor the stiffness degradation of the composite layer enabling progressive damage tracking.

4.2 Shear Failure in Isotropic Materials

The shear failure is described with a simple failure criterion that is suitable for dynamic problems and is based on von Mises stress and equivalent plastic strain [15]. Material yielding starts when von Mises stress reaches the allowable strength of isotropic materials. Then, it is assumed that failure occurs when the equivalent plastic strain corresponds to the failure strain of isotropic materials.

4.3 Material Properties

The materials used in the blade are balsa wood, UD-GF, GF fabric, and CF fabric. The balsa wood which follows an elastic-perfectly plastic behavior in the simulations has the Young's modulus of 4.1 GPa, Poisson's ratio of 0.3, yield strength of 5.4 MPa, failure strain of 0.8, and density of 155 kg/m^3 [4, 21]. The homogenized elastic properties of the composite materials are presented in Table 2, and their allowable strength and ultimate strain used to calculate energy dissipation of the composites are presented in Table 3 [22-24]. From Eq. (4), the energy dissipation is obtained as a factor of the characteristic length and is presented in Table 3. While von Mises yield criterion is utilized for the balsa wood, Hashin damage model is utilized for the composite materials.

5 Element and Mesh Selection

The blade is represented with Lagrangian S3R/S4R linear shell element of Abaqus, commercial finite element software. Thes elements has three displacement and three rotational degrees of freedom, allow finite strain, arbitrarily large rotation, and transverse shear, and are valid for thin and thick shell problems. The SW45 blade model with the combined coarse and fine meshes is created in HyperMesh. The fine mesh size of 0.02 m is employed in the 5 m tip-sectional blade while the coarse mesh size of 0.15 m is assigned for the rest of the SW45 blade (4 m < r < 75 m). This leads to disengaged nodes at r = 75 m. To overcome this disparity in the SW45 blade model, the coarse mesh region is tied to the fine mesh region at r = 75 m with the *TIE control. Total of 104,585 Lagrangian elements are generated for the SW45 blade model.

The mesh size of 0.01 m is applied for the Eulerian domain that contains the bird, generating 1,200,000 EC3D8R Eulerian elements. The Eulerian elements represent stationary rectangular grids and allow material to flow through the elements and to interact with the Lagrangian element structure. Eulerian elements overcome numerical difficulties associated with excessive element distortion since materials are assigned to them by means of volume fraction [15].

6 Preloads: Lift and Drag

The blade is subjected to aerodynamic, gravitational, inertial, and service loads in operation. Since mostly aerodynamic loads such as lift and drag forces contribute to the deformation of the blade, they are selected as preloads in the impact simulations. Lift (δL) and drag (δD) forces for the rotating blade calculated using two-dimensional airfoil characteristics are given by

$$\delta L / c\delta r = \rho_{air} V_{rel}^2 C_l / 2 \qquad (5)$$

and

$$\delta D / c\delta r = \rho_{air} V_{rel}^2 C_d / 2 \qquad (6)$$

Here, δr is the infinitesimal blade length; ρ_{air}, an air density; V_{rel}, resultant relative wind velocity; C_l, a lift coefficient; C_d, a drag coefficient [8]. Air

density is selected to reflect the tower height. Resultant relative wind velocity is formed by combining a tangential air flow velocity and wind speed (u_w) [8]. Lift and drag coefficient corresponding to the limit angle of attack (α_l) is selected to have the upper limit of C_l in a low-drag lift coefficient range [14]. A tip speed ratio (TSR) defined in Eq. (7) is introduced to determine angular velocity (Ω) [8, 25].

$$\mathrm{TSR} = R\Omega / u_w \tag{7}$$

Therefore, the resultant of each decomposed load component along the Y- (dP_Y) and Z-axis (dP_Z) become, respectively:

$$dP_Z = (\delta L / c\delta r)\cos\alpha + (\delta D / c\delta r)\sin\alpha \tag{8a}$$

and

$$dP_Y = -(\delta L / c\delta r)\sin\alpha + (\delta D / c\delta r)\cos\alpha \tag{8b}$$

Air density is assigned as 1.208 kg/m^3 for 140 m tower (hub) height. The TSR of the blade is assumed to be constant at 7 [25]. Since tangential velocity of the blade is not constant along the rotor radius, lift and drag forces are evaluated along eight sections and are applied to the blade[26, 27].

7 Bird Impact Models

In this study, four impact models are considered to understand the influence of preloading and boundary conditions to the structural response of the blade. The CEL approach is employed to simulate the bird impact problems in Abaqus/Explicit. In all models, the 2kg gel bird is considered as a soft body and modeled with Eulerian elements (EC3D8R). Due to the fixed Eulerian mesh, the boundary of the bird is recomputed in each time increment as it flows through the mesh. Accordingly, gelatin is assigned to Eulerian elements by means of Eulerian volume fraction (EVF) that represents the ratio by which each Eulerian element is filled. Volume fraction of 0 indicates that the elements are not filled at all (i.e., they constitute a void); on the contrary the volume fraction of 1 states that the elements are completely filled with gelatin as seen in Fig. 3 [15]. Thus, the bird is represented inside the Eulerian domain with a combination of fully and partially filled elements surrounded by void regions. A general contact algorithm, which automatically detects which surfaces and edges come into contact, with a penalty method and frictionless surface is employed in the simulations [12, 28].

7.1 Effect of Preloading

The 2kg-bird is located perpendicular to the rotational plane of a wind turbine at r = 77.5 m and impacts the lower blade skin of the 80 m blade model (SW45) with the combined coarse and fine meshes.

7.1.1 Impact Model IA

In this impact model, the blade is subjected to lift and drag forces produced at u_w = 9.5 m/s. Before the impact analysis, the blade undergoing these forces is analyzed in Abaqus/Standard (implicit) where the three rotations and three displacements are constrained at the blade root.

The deformed blade that contains the values of stress, strains, displacements, etc obtained at u_w = 9.5m/s (Fig. 4) is imported into a new analysis (explicit) with the *IMPORT option. Then, the angular velocity (ω_z) of 0.824 rad/s about the Z-axis, generated by u_w = 9.5 m/s, is assigned to account for the centrifugal forces. At this stage, the bird has a translational velocity of 24.5 m/s along the Z-axis, which consists of the bird velocity of 15 m/s and wind speed of 9.5 m/s.

7.1.2 Impact Model IB

Since wind speed of 0 m/s is assumed in this impact model, the blade is not subjected to any aerodynamic loads and thus it is not deformed and remains straight (Fig. 5). For comparison purpose, it is assumed that the blade is rotating about the Z-axis with angular velocity of 0.824 rad/s. The initial velocity of the bird along the Z-axis is assigned as 15 m/s.

7.2 Effect of the Target Structure Size

Oblique impact scenarios are considered, and the impact location is at r = 77.5 m. The bird is initially located at an impact angle of 30° to the lower forward blade skin. The initial velocity along the Y- and the Z-axis is assigned as 70.5 m/s and 40.7 m/s, respectively.

7.2.1 Impact Model IIA

The Lagrangian target structure for the bird is the 5m tip-section of the 80 m blade (TSB5M blade) modeled with S4R shell elements and mesh size of 0.02 m. The edges of the blade at r = 75 m are fully constrained. No initial displacements and stresses are applied to the target structure.

7.2.2 Impact Model IIB

The SW45 blade model is employed as the target. The three rotation and three displacement degrees of freedom (DOF) are constrained at the blade root. The blade is not subjected to any aerodynamic loads.

8 Results and Discussion

8.1 Bird impact with and without Preloads

The 2kg-bird, originally located at r = 77.5 m, hits the lower blade skin of the blade which is rotating with ω_z = 0.824 rad/s. Before the bird impact, the preloaded blade experiences non-zero initial states due to lift and drag forces at u_w = 9.5 m/s.

8.1.1 Displacements

Since the bird is traveling along the Z-axis, U_3 displacements are critical in the impact problem. Global U_3 displacement contours in the lower blade skin of the preloaded blade are presented in Fig. 6. The displacement of 4.72 m is generated at r = 75 m due to preloading, and its magnitude increases to 5.63 m toward the tip at time (t) of 0 s. After the impact occurs, the magnitude of U_3 displacements does not change at t = 0.010 s signaling that the displacements produced by impact are much smaller than those due to preloading.

For the blade without any preloads, it is seen in Fig. 7(a) that the maximum value for global U_3 displacements in the impact site is 2.51×10^{-3} m and is located in the lower forward blade skin at t = 0.001 s. Since impact site varies with time due to the blade rotation and flying bird, the greatest U_3 displacement (9.07×10^{-3} m) is in the skin/spar cap at t = 0.010 s, as seen in Fig. 7(b). The negative values of the displacements are distributed in the aft blade skin. At t = 0.0125 s, the greatest displacement of 6.61×10^{-3} m is generated in the skin/spar cap while the negative displacement of 4.03×10^{-3} m is seen in the aft skin as illustrated in Fig. 7(c). This displacement development arises from wave propagation and local fluctuations produced by the impact.

8.1.2 Stresses

Mostly, the S_{22} stresses contribute to the layer damage [29]. The outermost GF fabric layer of the lower skin in the preloaded blade (75 m < r < 80 m) experiences S_{22} stress in a range of - 6.50 MPa and 8.49 MPa at t = 0 s as presented in Fig. 8(a). Then, the stress increases to -67.6 MPa at the impact site at t = 0.001 s. The compressive S_{22} stress drops when the impact site expands from the skin to the skin/spar cap. Its maximum value is 47.1 MPa in the skin/spar cap at t = 0.010 s as seen in Fig. 8(c). Also, the tensile S_{22} stress of 72.8 MPa is present around the boundary between the aft skin and skin/spar cap. This high tensile stress around the boundary is attributed to the stiffness discontinuity of the laminates between the aft skin and skin/spar cap. Compressive S_{22} stresses are distributed the region surrounding the impact site.

Although the blade without preloads does not exhibit initial stresses due to the lift, drag, and centrifugal forces at t = 0 s, it is subjected to the same magnitude of centrifugal forces during the impact. Its S_{22} stress field in the outermost GF fabric of the lower skin at t = 0.001 s is presented in Fig. 9(a) where the lowest S_{22} stress of -52.5 MPa is seen at the impact site, and the highest S_{22} stress (58.9 MPa) appears around the boundary between the forward skin and skin/spar cap. At t = 0.010 s, the maximum value for the compressive and tensile S_{22} stress are 38.5 MPa and 48.1 MPa, respectively, as presented in Fig. 9(b).

Note that both cases (with and without preloads) exhibit the same order of magnitude in S_{22} stresses which are considerably lower than material allowables of the composite layers and the core. Also note that the impact site remains localized. However, the preloaded blade showed stronger influence of impact wave propagation.

8.2 Bird impact on 5 m vs. 80 m blade

The 2kg-bird with two translational velocity components impacts the stationary target of (a) the 5m tip-sectional blade (TSB5M) and (b) full-length 80 m blade (SW45). Neither blade is preloaded in these simulations.

8.2.1 Energy Balance

Kinetic energy balance of Impact Model IIA (TSB5M blade/bird) and IIB (SW45 blade/bird) is presented in Fig. 10. The kinetic energy balance for both the models agreed well as a function of time. The initial kinetic energy of 6.64 kJ produced by the flying bird decreased to 5.25 kJ at 0.006 s. This energy loss (1.39 kJ) is represents both deformation of the blade and energy dissipation during the impact. Although the contact between the bird (gel) and the blade is terminated at 0.0085 s, mostly the interaction between the gel and the blade takes place between 0.0015 s and 0.006 s. The leakage of the gel

transpires after 0.008 s causing a decrease in kinetic energy. However, this decrease is not significantly important since the gel moving out from the domain does not interact with the blade.

The internal energy balance of both impact models is presented in Fig. 11. This energy consists of the recoverable strain energy of the blade and Eulerian domain, and the energy dissipated by yielding and damage. Initially, the internal energy increases to 1.02 kJ due to the impact, and then it approaches 0.95 kJ due to elastic recovery. The discontinuous path of the energy balance occurs around 0.004 s when the first failure region is observed in the blade. In spite of different size and boundary conditions, the internal energy balance is quite consisted between these models. It is noted that the size of the bird is much smaller in comparison to the global dimensions of the blade such as the blade tip radius and chord length.

9 Conclusions

The reinforcement architecture and geometry successfully survived the realistic bird impact event (implicit-explicit coupling) without incurring any damage in the composite layers and the balsa core of the hybrid composite turbine blade. The differences in the boundary conditions, preloads and full vs. sectional blade configurations did not alter the computational impact response. Thus it is advisable to adopt the smaller 5m tip-sectional blade for impact experiments.

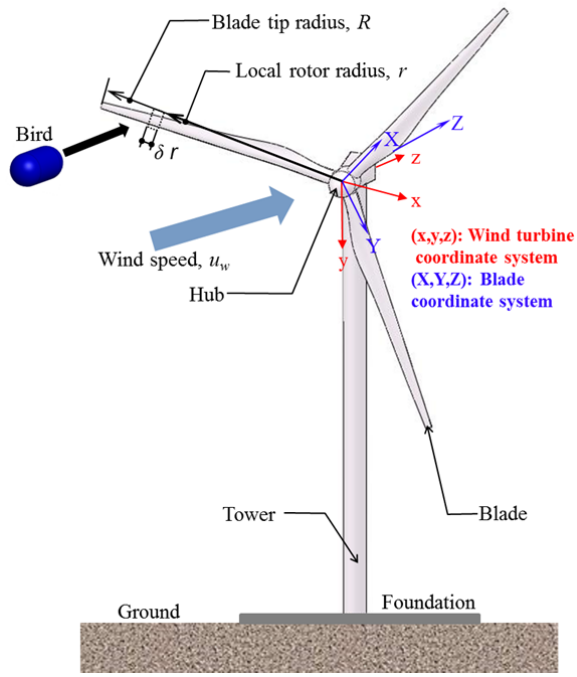

Fig. 1. Schematic of a typical wind turbine.

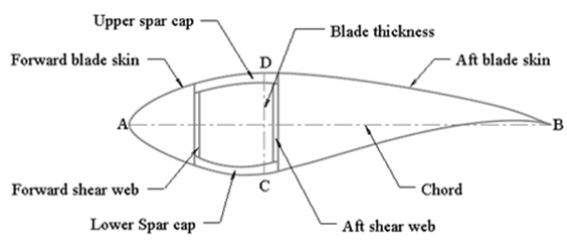

Fig. 2. Cross-section of the typical blade.

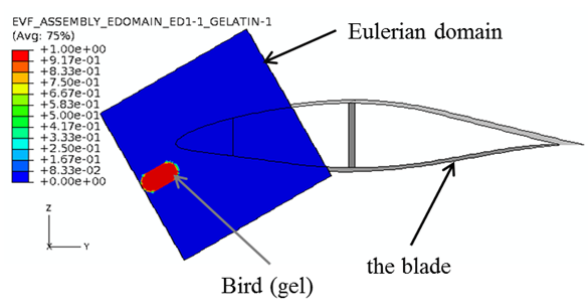

Fig. 3. EVF representation of the bird.

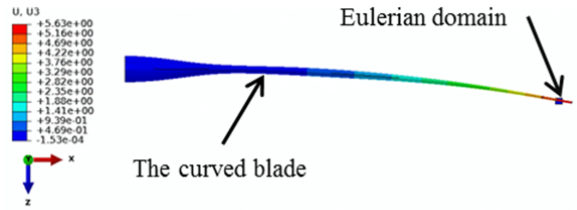

Fig. 4. The blade with preloads before bird impact.

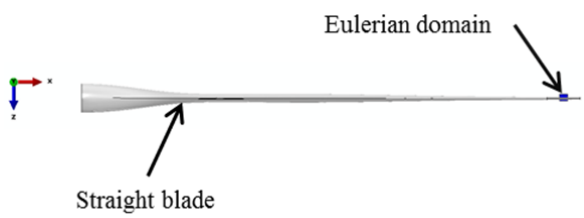

Fig. 5. The blade without preloads before bird impact.

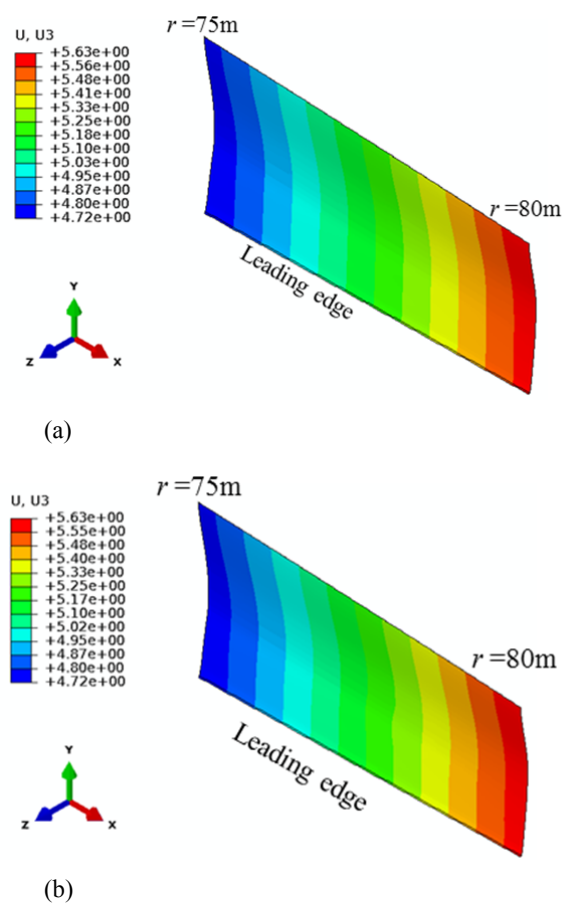

Fig. 6. U_3 displacements in the lower blade skin of the blade with preloads (75 m < r < 80 m): (a) 0 s, and (b) 0.010 s.

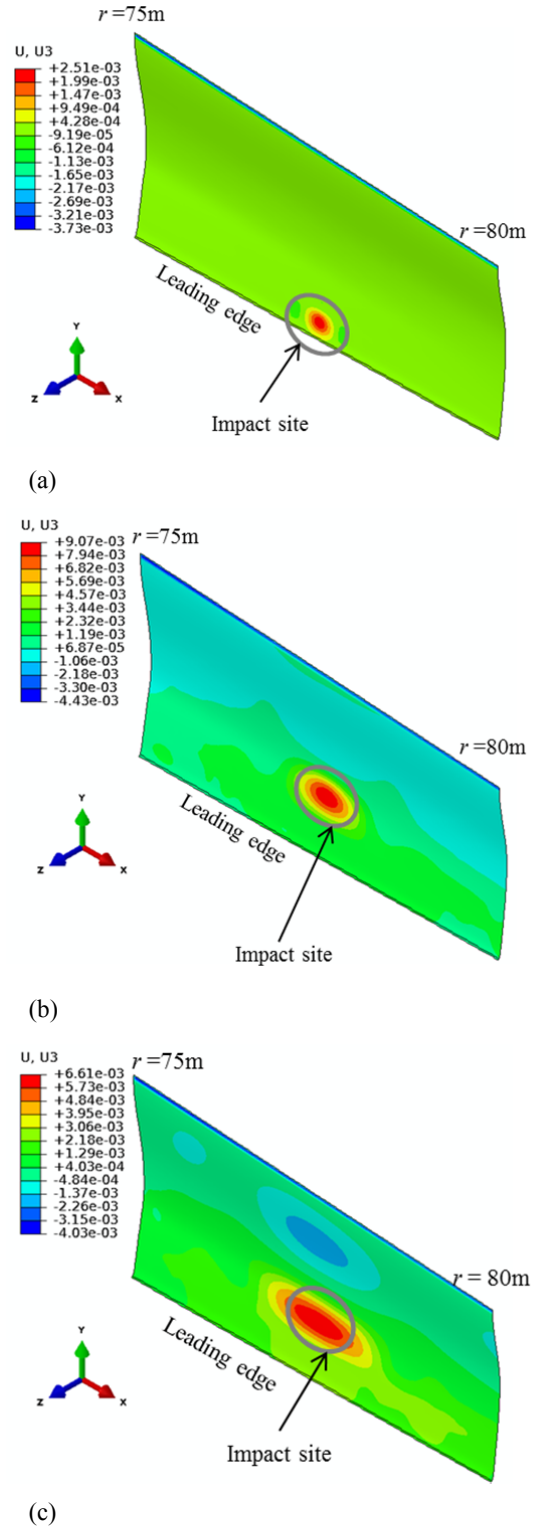

Fig. 7. U_3 displacements in the lower blade skin of the blade without preloads (75 m < r < 80 m): (a) 0.001 s, (b) 0.010 s, and (c) 0.0125 s.

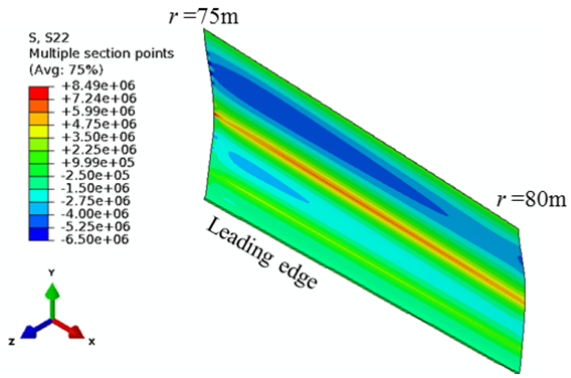

(a)

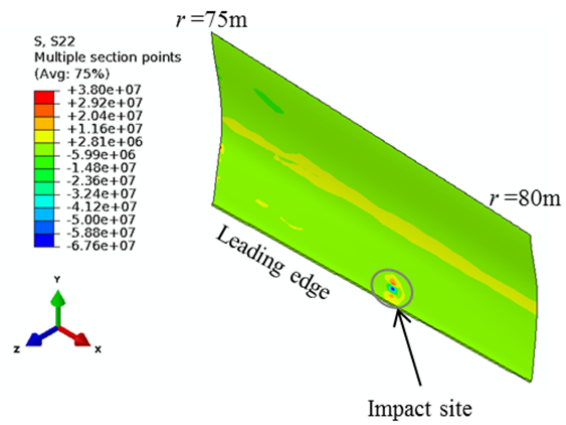

(b)

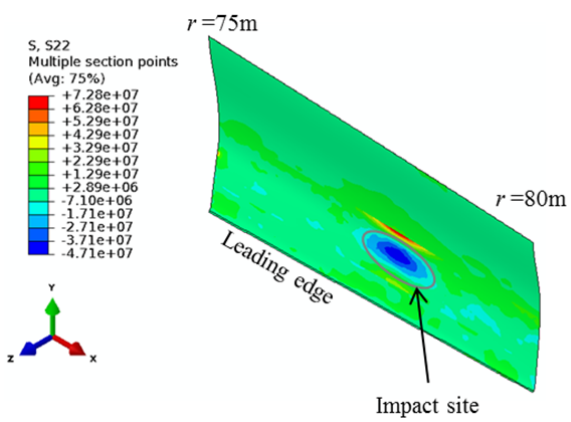

(c)

Fig. 8. S_{22} stress in the outermost GF fabric of the lower skin of the blade with preloads (75 m < r < 80 m): (a) 0 s, (b) 0.001 s, and (c) 0.010 s.

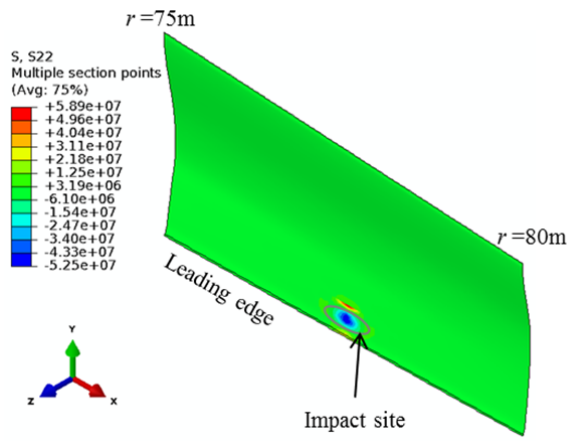

(a)

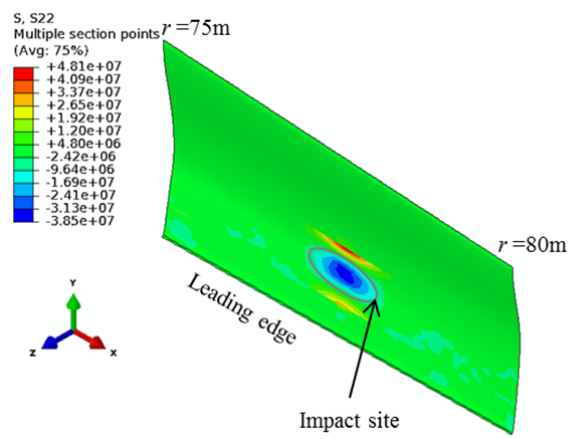

(b)

Fig. 9. S_{22} stress in the outermost GF fabric of the lower skin of the blade without preloads (75 m < r < 80 m): (a) 0.001 s, and (b) 0.010 s.

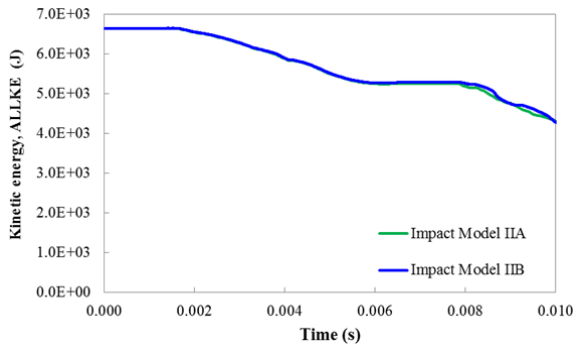

Fig. 10. Kinetic energy balance of impact model IIA and IIB.

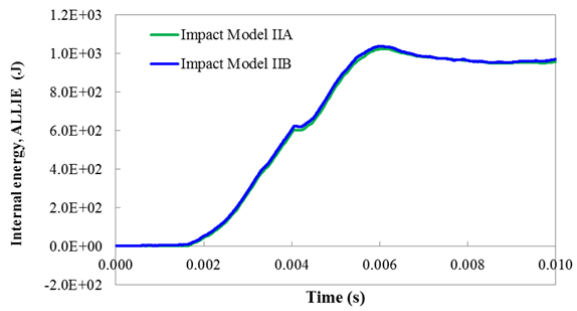

Fig. 11. Internal energy balance of impact model IIA and IIB.

Table 1. Thickness distribution in the airfoil section in meter.

Range of local rotor radius	Face sheet thickness	Balsa core thickness			Spar cap
		Forward blade skin	Aft blade skin	Shear web	
5.6-20	0.002	0.032	0.054	0.054	0.074
20-32	0.002	0.036	0.060	0.060	0.036
32-46	0.002	0.030	0.050	0.050	0.029
46-60	0.001	0.020	0.044	0.032	0.022
60-70	0.001	0.016	0.035	0.025	0.016
70-75	0.001	0.013	0.029	0.021	0.012
75-80	0.001	0.011	0.025	0.018	0.009

Table 2. Linear elastic properties of composite materials.

	UD-GF	GF fabric $[0/90]_s$	CF fabric $[0/90]_s$
ρ_m (kg/m^3)	2,100	2,100	1,600
E_1 (GPa)	46	21	47
E_2 (GPa)	13	21	47
E_3 (GPa)	13	8.55	10
G_{12} (GPa)	5	3.7	3.78
G_{13} (GPa)	5	3.5	3.5
G_{23} (GPa)	4.6	3.5	3.5
v_{12}	0.3	0.183	0.33
v_{13}	0.3	0.0305	0.33
v_{23}	0.42	0.075	0.07

Table 3. Allowable strength, strain, and energy ratio.

	UD-GF	**GF fabric [0/90]s**	**CF fabric [0/90]s**
X_T/X_C (MPa)	1,080/620	367/549	627/572
Y_T/Y_C (MPa)	39/128	367/549	627/572
S_L/S_T (MPa)	89/64	97.1/274.5	80/286
$\varepsilon_{1t}^f/\varepsilon_{1c}^f$ (%)	2.8/0.5	2.5/2.5	1.5/1.5
$\varepsilon_{2t}^f/\varepsilon_{2t}^f$ (%)	2.8/0.5	2.5/2.5	1.5/1.5
G_{ft}^C/G_{fc}^C ($\times 10^6$ N/m)	(15.1/1.55)$\times L_c$	(4.59/6.86)$\times L_c$	(4.70/4.29)$\times L_c$
G_{mt}^C/G_{mc}^C ($\times 10^6$ N/m)	(0.546/0.320)$\times L_c$	(4.59/6.86)$\times L_c$	(4.70/4.29)$\times L_c$

References

[1] C.B. Hasager, A. Peña, T. Mikkelsen, M.S. Courtney, I. Antoniou, S.E. Gryning, et al. "*12MW horns rev experiment*". Risø National Laboratory, 2007: Riso-R-1506(EN).
[2] D.A. Griffin "*WindPACT turbine design scaling studies technical area 1: composite blades for 80-to 120-meter rotor*". National Renewable Energy Laboratory, 2001: NREL/SR-500-29492.
[3] O.T. Thomsen "Sandwich materials for wind turbine blades - present and future". *J Sandw Struct Mater*, Vol. 11, No. 1, pp 7-26, 2009.
[4] A. Todoroki and Y. Kawakami "Optimal design of wind turbine blade of CF/GF hybrid composites". *Trans JSCES* Vol. 2008, No. 2008, pp 20080012, 2008 [in Japanese].
[5] M.H. Mohamed and K.K. Wetzel "3D woven carbon/glass hybrid spar cap for wind turbine rotor blade". *J Sol Energ - T Asme*, Vol. 128, No. 4, pp 562-573, 2006.
[6] D.A. Griffin "*Blade system design studies volume I: composite technologies for large wind turbine blades*". Sandia National Laboratories, 2002: SAND2002-1879.
[7] D.A. Griffin "*Blade system design studies volume II: preliminary blade designs and recommended test matrix*". Sandia National Laboratories, 2004: SAND2004-0073.
[8] T. Burton, N. Jenkins, D. Sharpe and E. Bossanyi "*Wind energy handbook*". Wiley, 2011.
[9] L.M.L. Castelletti and M. Anghileri "Multiple birdstrike analysis - a survey of feasible techniques". *Proceedings of the 30th European Rotorcraft Forum*, Marseilles, pp 495-505, 2003.
[10] S. Heimbs "Computational methods for bird strike simulations: a review". *Comput Struct*, Vol. 89, No. 23-24, pp 2093-2112, 2011.
[11] S. Heimbs "Bird strike simulations on composite aircraft structures". *Proceedings of 2011 SIMULIA Customer Conference*, Barcelona, pp 73-86, 2011.
[12] Y. Shmotin, P. Chupin, D. Gabov, A. Ryabov, V. Romanov, S. Kukanov, et al. "Bird strike analysis of aircraft engine fan". *Proceedings of the 7th European LS-DYNA Conference*, Salzburg, H-I-03, 2009.
[13] S. McCallum and C. Constantinou "The influence of bird-shape in bird-strike analysis". *Proceedings of the 5th European LS-DYNA Users Conference*, Birmingham, 2c-77, 2005.
[14] D. Somers "*The S816, S817, and S818 airfoils*". National Renewable Energy Laboratory, 2004: NREL/SR-500-36333.
[15] ABAQUS, Inc "*ABAQUS documentation collection, Version 6.12*". ABAQUS, Inc., 2012.
[16] A. Airoldi and B. Cacchione "Modelling of impact forces and pressures in Lagrangian bird strike analyses". *Int J Impact Eng*, Vol. 32, No. 10, pp 1651-1677, 2006.
[17] A.F. Johnson and M. Holzapfel "Modelling soft body impact on composite structures". *Compos Struct*, Vol. 61, No. 1-2, pp 103-113, 2003.
[18] Z. Hashin "Failure criteria for unidirectional fiber composites". *J Appl Mech -T Asme*, Vol. 47, No. 2, pp 329-334, 1980.
[19] Z. Hashin and A. Rotem "A fatigue failure criterion for fiber reinforced materials". *J Compos Mater*, Vol. 7, No. 4, pp 448-464, 1973.
[20] I. Lapczyk and J.A. Hurtado "Progressive damage modeling in fiber-reinforced materials". *Compos Part A*, Vol. 38, No. 11, pp 2333-2341, 2007.
[21] M. Vural and G. Ravichandran "Microstructural aspects and modeling of failure in naturally occurring porous composites". *Mech Mater*, Vol. 35, No. 3-6, pp 523-536, 2003.
[22] M.D. Daniel and O. Ishai "*Engineering mechanics of composite materials*". Oxford University Press, 1994.
[23] C. Kyriazoglou and F.J. Guild "Finite element prediction of damping of composite GFRP and CFRP laminates: a hybrid formulation–vibration damping experiments and Rayleigh damping". *Compos Sci Technol*, Vol. 66, No. 3-4, pp 487-498, 2006.
[24] MatWeb Greene tweed orthetek WF polyketone, continuous woven carbon fiber, Database of material properties. http://www.matweb.com/search/QuickText.aspx?SearchText=woven%20carbon. Accessed 12 January 2010.
[25] E. Hau "*Wind turbines: fundamentals, technologies, application, economics*". 2nd edition, Springer-Verlag, 2006.
[26] N. Nanami "*Vibration and structural response of hybrid wind turbine blades*". Master's thesis, Texas A&M University, 2010.
[27] N. Nanami and O.O. Ochoa "Vibration and dynamic response of hybrid wind turbine blades". In: Liu D, editor. *Dynamic effects in composites materials*, Vol. 1. Lancaster: DEStech Publications; 2012. pp 289-301.
[28] D.J. Benson and S. Okazawa "Contact in a multi-material Eulerian finite element formulation". *Comput Method Appl M*, Vol. 193, No. 39-41, pp 4277-4298, 2004.
[29] N. Nanami and O.O. Ochoa "Computational assessment of bird strike on hybrid composite wind turbine blade". *Proceedings of the American Society for Composites 27th Annual Technical Conference*, Arlington, 245, 2012.